Journal of Electroanalytical Chemistry 760 (2016) 42–47

Contents lists available at ScienceDirect

Journal of Electroanalytical Chemistry

journal homepage: www.elsevier.com/locate/jelechem

Electrochemical redox cycling in a new nanogap sensor: Design and simulation

Hamid Reza Zafarani [a], Klaus Mathwig [b], Ernst J.R. Sudhölter [a], Liza Rassaei [a,*]

[a] Laboratory of Organic Materials and Interfaces, Department of Chemical Engineering, Delft University of Technology, Julianalaan 136, 2628 BL Delft, The Netherlands
[b] Pharmaceutical Analysis, Groningen Research Institute of Pharmacy, University of Groningen, P.O. Box 196, 9700 AD, Groningen, The Netherlands

ARTICLE INFO

Article history:
Received 2 October 2015
Received in revised form 22 November 2015
Accepted 23 November 2015
Available online 02 December 2015

Keywords:
Redox cycling
Electrochemical sensor
Nanogap sensor
Microfluidic sensor
Finite element method

ABSTRACT

We propose a new geometry for nanogap electrochemical sensing devices. These devices consist of two closely spaced side-by-side electrodes which work under redox cycling conditions. Using finite element simulations, we investigate the effects of different geometric parameters on the redox cycling signal amplification to gain insight into the electrochemical sensing performance of the device design. This will allow optimizing the sensor performance of devices to be fabricated in the future.

1. Introduction

Micro/nanoelectrode systems have been extensively studied for electrochemical (bio)sensing applications due to their fast response time, small capacitive currents and steady-state voltammetric response, which compare favorably to macroelectrode systems [1]. However, the small surface area of these electrodes limits their sensitivity, in particular at low analyte concentrations, due to the limited sensitivity of electronic instrumentation [2]. One way to circumvent these limitations is to configure the electrodes in a dual mode, thereby taking advantage of redox cycling between them. In this way, the concentration profiles of both species overlap, allowing the species generated at one electrode to be efficiently collected at the other electrode. Such successive oxidation and reduction of analyte molecules as a result of the inter-diffusion between two closely spaced electrodes lead to current amplification and, thus, the detection limit of electrochemical sensors is lowered [3–5]. These systems are a modified version of rotating ring disc electrodes operating in generator–collector mode which were in particular developed by Albery and Hitchman [6,7] followed by the development of numerous electrode geometries and techniques such as double-band channel electrodes [8], micro-ring-disc electrodes [9], micro-electrode arrays [10], interdigitated electrodes [11], dual microdisc electrodes [12], and junction electrodes [13]. A summary of the variety of geometries and applications can be found in reference [14].

The advantages of the redox cycling devices are not only limited to an improvement of the sensor sensitivity by amplification of faradic currents [11,15]; they are also powerful tools for determining diffusion coefficients of redox species [8,16] and monitoring the lifetime of electrogenerated intermediates [17,18]. One widely used type of redox cycling devices is thin layer cells which consist of two planar electrodes separated by a thin layer of liquid [19]. Recently, Marken *et al.* developed a simple method for the preparation of dual-plate electrode systems with a micrometer gap *via* etching a thin epoxy layer between the two electrodes [20–22]. Despite the advantage of a simple and innovative fabrication methodology, the gap size is limited to the micrometer length scale, and the method is not compatible mass fabrication needed for many practical applications. The sensitivity of any thin layer cell sensor is increased by reducing the gap size between the two electrodes [21]. However, reducing the gap size to the nanometer range requires cleanroom facilities and multi-step photo or e-beam lithography techniques [19] as demonstrated in pioneering works by Lemay *et al.* [23,24]. In this approach, nanogap devices are fabricated layer-by-layer. Subsequent to the microfabriation, a sacrificial chromium layer separating to metal electrodes is wet-etched, creating a nanochannel and completing the formation of the nanogap sensor. The sensitivity of these nanogap devices allows even single-molecule detection [25,26], and they have been used for a variety of applications [24,27,28]. Considering the need for more sensitive sensing devices, there exists a demand for new nanogap sensors which are simpler to fabricate. Various geometries and fabrication method have been suggested in last few years [4,29]. We currently aim at the fabrication of a new type of nanogap sensor consisting of two closely spaced side-by-

* Corresponding author.
E-mail address: l.rassaei@tudelft.nl (L. Rassaei).

http://dx.doi.org/10.1016/j.jelechem.2015.11.031
1572-6657/

side electrodes. Comparable redox-cycling sensors with side-by-side electrodes have been realized by a variety of fabrication methods using different electrode materials [30–32]. All of these sensors employ side-by-side electrodes in interdigitated geometries. However, they operate in a microscale regime with gap sizes above 1 μm and, thus, do not benefit from the unique advantages of nanoscale sensors such as highest amplification factors. Side-by-side interdigitated electrodes with submicrometers distances have been fabricated, but only employed for impedance sensing [33].

In the present work, we employ numerical finite element simulations to study the electrochemical sensing behavior in a new nanogap design. By evaluating the influence of geometric parameters as well as electrode potentials on the sensor performance an understanding of design rules is gained for future device fabrication.

2. Methods

2.1. Sensor geometry

The nanogap sensor consists of two closely spaced electrodes positioned next to each other (see Fig. 1). The top sides of both electrodes are passivated to avoid a contribution to the electrochemical signal.

COMSOL Multiphysics (version 4.4) was employed to simulate the electrochemical processes and mass transport of analytes in the nanogap sensor. We assume an unstirred solution (with the exception of Section 3.5) and a high supporting electrolyte concentration. Therefore mass transport is diffusive, and convection and migration are not considered. The effects of various design parameters, namely the gap size, the thickness of the top isolating layer, the electrode thickness, the collector potential and the flow rate (see Section 3.5) were studied, and their influence on the current signal and the signal amplification factor was determined.

The geometry of the device allows simplifying the simulation to a two-dimensional geometry. Fick's second law describes diffusion of species:

$$\frac{\partial C_j}{\partial t} = D_j \nabla^2 C_j. \tag{1}$$

C_j and D_j are the concentration and diffusion coefficient of a redox species j. For simplicity, we consider equal diffusion coefficients for both oxidized and reduced species (see Table 1).

2.2. Electrochemical reactions

The archetypical redox reaction

$$Fc(MeOH)_2^+ + e^- \underset{k_b}{\overset{k_f}{\rightleftharpoons}} Fc(MeOH)_2 \tag{2}$$

was simulated at the electrode surfaces. k_f and k_b are as the forward (reduction) and backward (oxidation) rate constants. The current was defined based on Butler–Volmer kinetics as [34].

$$i = nF[c_O k_b - c_R k_f] \tag{3}$$

Table 1
Constants used in the current simulation processes [23,29].

D_O	6.7×10^{-10} m^2/s	α	0.49
D_R	6.7×10^{-10} m^2/s	F	96,485 C/mol
k_0	0.06 m/s	R	8.31 J/K
E_{std}	0.251 V *vs.* Ag/AgCl	T	298 K

$$k_f = k_0 \exp\left[\frac{-\alpha F\,(E - E_{std})}{RT}\right] \tag{4}$$

$$k_b = k_0 \exp\left[\frac{(n-\alpha) F\,(E - E_{std})}{RT}\right] \tag{5}$$

Here, k_0 is the 'standard electrochemical rate constant', α: 'transfer coefficient', F: Faraday constant, E: electrode potential, E_{std} standard potential of the redox couple, n: number of electrons transferred in the redox reaction, c_O and c_R concentration of the oxidized and reduced species, respectively.

2.3. Model geometry

In our simulation, two electrodes are considered with variable thicknesses and a 3 μm width (*i.e.*, the length of the gap in the third dimension which is not simulated explicitly). The electrodes are located at close distance next to each other. An isolating layer is considered above each electrode with a defined thickness. Finally, a solution containing 1 mM $Fc(MeOH)_2$ in fills the gap and a reservoir above the device. All potentials are defined *versus* a Ag/AgCl reference electrode.

Table 1 lists the value of the constants used in the simulation based on experimental values reported in the literatures [23,29]. However, the choice of the electrolyte as well as the electrode material and electrode surface conditions can affect these constants [23,35]. In all dual mode studies, the right electrode (generator) was swept in the potential range of 0–0.5 V *vs.* Ag/AgCl, while the left electrode (collector) was kept constant at a cathodic potential (0 V, except for studying the effect of varied collector potentials, see Section 3.4). Under these conditions, the oxidized species are produced at the generator electrode, the majority of this species is reduced again at the collector electrode and then diffuses back to the generator electrode for re-oxidation.

3. Results and discussion

3.1. Study of the gap size

One important feature in the design of nanogap sensors is the distance between the two electrodes [28,36]. Reducing the gap size enhances the current amplification due to a shorter diffusion time between the two electrodes [23,37]. Thus, we studied this effect on the current amplification factor, which we defined as the ratio between the generator limiting current in dual mode to the current in single mode. (As shown in the cyclic voltammograms in Fig. 2B, the single-

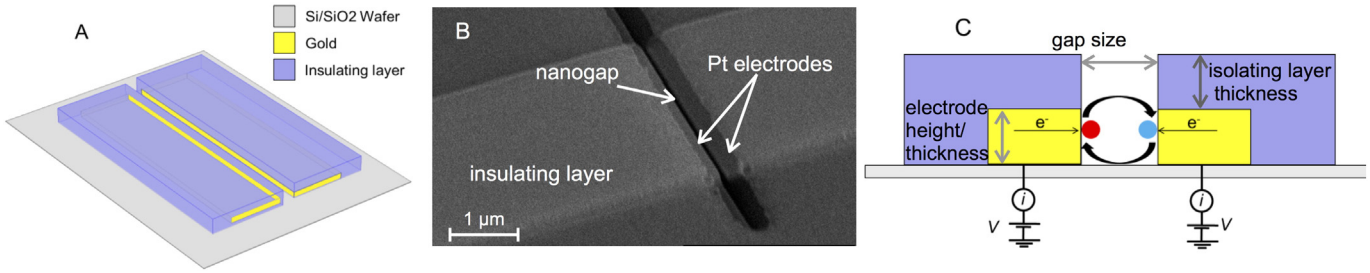

Fig. 1. (A) Schematic of the proposed nanogap sensor, (B) scanning electron micrograph of a precursor of a device acquired at a 30° angle, and (C) schematic side view.

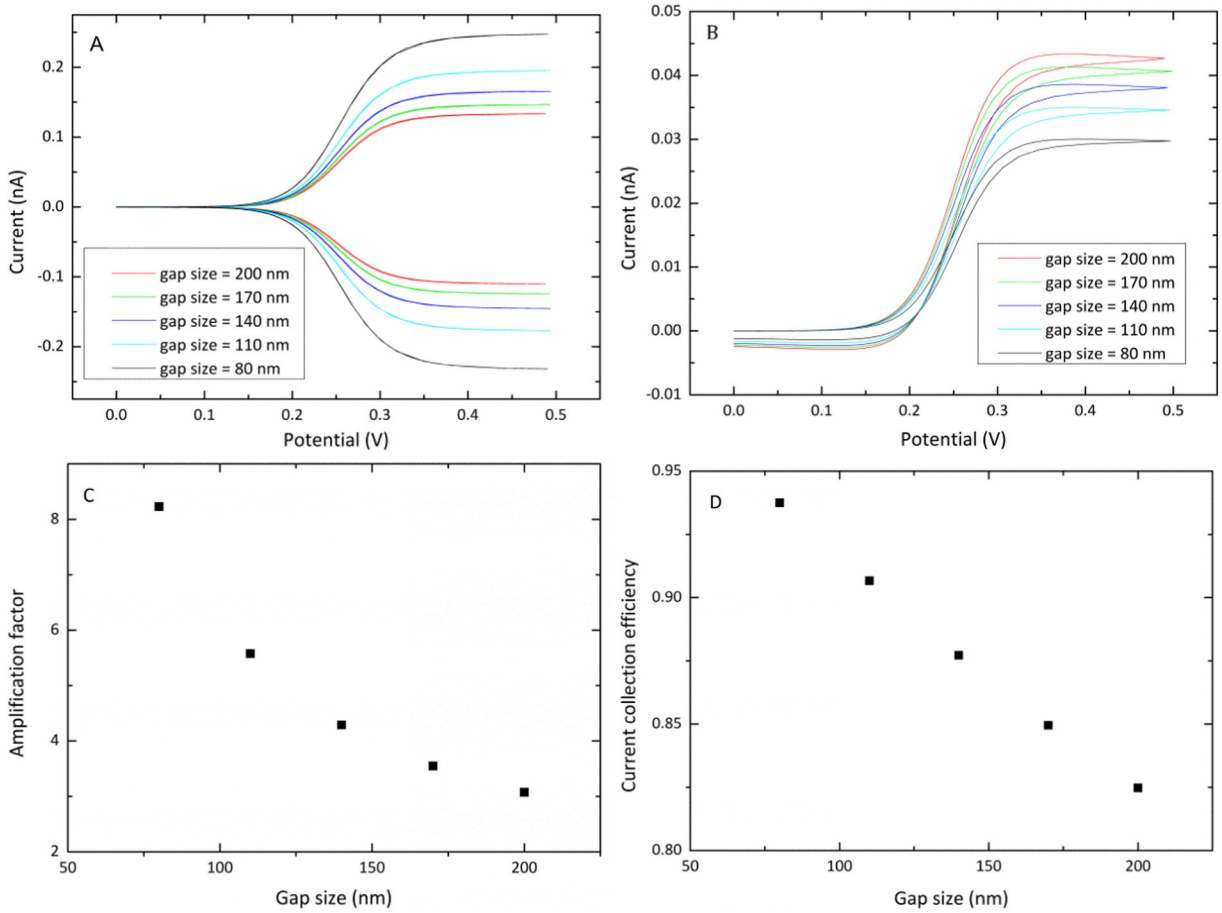

Fig. 2. (A) Simulated cyclic voltammograms (scan rate = 10 mVs^{-1}) showing the effect of the distance between the two electrodes (gap size) in redox cyclic mode (the generator electrode was swept between 0 and 0.5 V while the collector potential was kept constant at 0 V). (B) Cyclic voltammograms (scan rate: 10 mVs^{-1}) showing the effect in single mode (one electrode was swept between 0 and 0.5 V while the other electrode was kept floating). (C) Plot showing the change in current amplification factor *versus* gap size in redox cyclic mode, and (D) plot showing the current collection efficiency *versus* the gap size in redox cyclic mode.

mode currents exhibit a slight hysteresis due to slow diffusion into the nanogap. We approximated the limiting current by the current at a potential of 0.5 V.) We also studied the effect on the collection efficiency (defined as the current ratio of the collector electrode to the generator electrode in dual mode; collection efficiency = $I_{collector}/I_{generator}$). In these simulations, the electrodes' thickness was chosen as 80 nm and the thickness of the top isolating layer was kept constant (250 nm). We simulated cyclic voltammograms of $Fc(MeOH)_2$ for different gap sizes (80 to 200 nm). As shown in Fig. 2A, decreasing the gap size results in an increase in both anodic and cathodic limiting current in agreement with reports in the literature. This increase is due to a reduced diffusion path between the two electrodes and, thus, more efficient redox cycling [28]. Fig. 2B presents simulated cyclic voltammograms for varied gap sizes in single mode. Interestingly, in single mode a decrease in current is found with decreasing gap size; this is attributed to slower diffusive transport from the reservoir into the narrower nanochannel. As

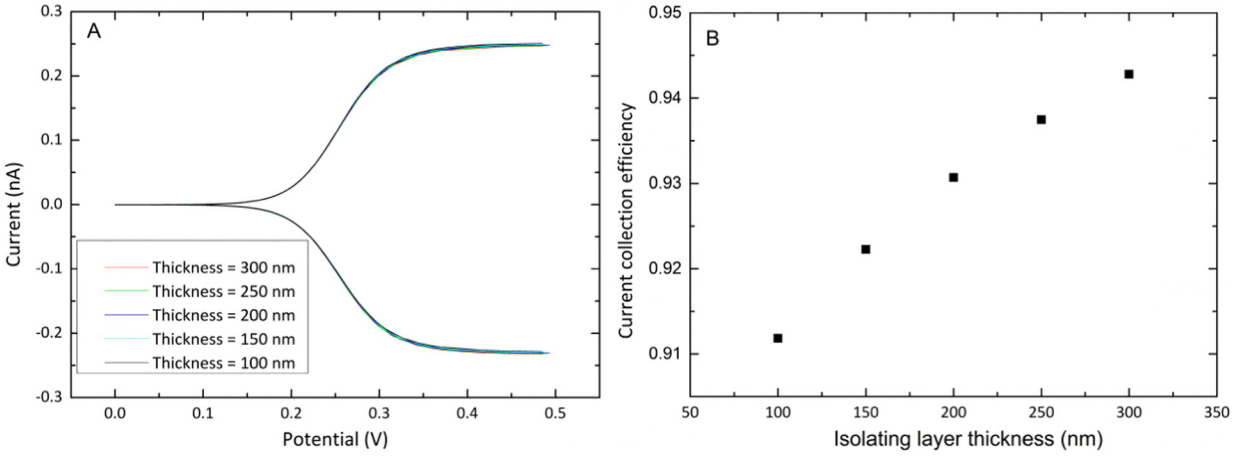

Fig. 3. (A) Cyclic voltammograms (scan rate: 10 mV s^{-1}) showing the effect of the isolating layer thickness on the current obtained in the redox cycling mode. (B) Current collection efficiency *versus* different isolating layer thicknesses in redox cyclic mode. (The generator electrode was swept between 0 and 0.5 V, and the collector potential was kept constant at 0 V).

shown in Fig. 2C and D, decreasing the gap size results in both a higher amplification factor and a higher current collection efficiency in dual mode.

3.2. Study of the isolating layer thickness

The role of the top isolating layer thickness was studied by varying the thickness in the range of 100 nm to 300 nm for a 80 nm wide nanogap (electrode layer thickness = 80 nm). Here, again, the potential of one electrode was swept from 0 to 0.5 V (scan rate of 10 mV s^{-1}) while the potential of the other electrode was kept constant at 0 V for the oxidation and reduction of 1 mM $Fc(MeOH)_2$. As shown in Fig. 3A, a change in the thickness of the top isolating layer does not affect the magnitude of the limiting current in dual mode, whereas increasing the isolating layer thickness from 100 nm to 300 nm decreases the limiting current in single mode from 0.045 nA to 0.025 nA (data not shown). This demonstrates that the diffusive access to the electrodes is slowed down by a thick isolating layer; however, this has no influence on the redox cycling efficiency as species between the two electrodes undergo repeated electron transfer processes.

Fig. 3B shows the trend of increasing current collection efficiency with increasing thickness of the top isolating layer due to the confinement of the redox species in the nanogap. Hence, the probability for diffusion of active species in the nanochannel back into the bulk reservoir decreases by increasing the thickness of the nanogap trench.

3.3. Study of the electrode thickness

Originally Anderson and Reilley estimated the limiting current I for two planar electrodes separated by a thin layer of fluid by the equation [37]

$$I = \frac{nFADC}{z}. \quad (6)$$

Here A is the overlapping area between the two electrodes, and z is distance between the electrodes (gap size). Thus, by increasing the electrode surface areas the redox cycling current is increased. We studied the influence of the electrode surface areas in the our nanogap design by varying their height (layer thickness) in the range from 30 to 130 nm in a device with a 80 nm gap size and a 250 nm isolating layer on top (see Fig. 4).

Increasing the electrode thickness from 30 to 130 nm enhanced the limiting current from 0.1 to 0.38 nA linearly (in agreement with Eq. (6)). As shown above in Fig. 3A, an enhanced species trapping due to the elevated electrodes does not improve the redox cycling current.

3.4. Study of the collector potential

In addition to the geometric parameters of the nanogap design we investigated the effect of the collector potential on the redox cycling current. We kept the collector electrode potential constant and values ranging from −0.5 to 0.2 V while the generator electrode potential was swept between 0 and 0.5 V in a 80 nm nanogap device with a 250 nm isolating layer thickness and an 80 nm electrode thickness. The effect of these changes on the cyclic voltammograms is shown in Fig. 5.

The concentration profiles in the nanogap device are shown in Fig. 6 for two different collector potentials. When the collector potential is set at 0.2 V, close to the half-wave potential, a small amount of $Fc(MeOH)_2^+$ is reduced at the collector electrode which results in a decrease in redox cycling current. However, by shifting the potential of the collector electrode to a more cathodic potential, more $Fc(MeOH)_2^+$ ions are reduced at the electrode and diffuse to the generator electrode where they are re-oxidized resulting in an increase in the limiting current. Further decreasing the potential of the collector electrode from 0 to −0.5 V does not affect the redox cycling current (see Fig. 5). This indicates that a potential of 0 V suffices to reduce the species produced at generator electrode back to its initial state. Such high overpotentials ensure that charge transfer does not limit the reaction rate [38].

3.5. Study of the flow rate

Contributions of both migration and convection to analyte mass transport were neglected in the simulations presented above. The proposed device can be implemented as a detection element in a microfluidic channel for improved sensitivity in microanalytical systems.

In microanalytical systems employing microelectrodes, the magnitude of the current typically depends on the solution flow rate, and the obtained signal has to be normalized to the hydrodynamic flow velocity. This is due to a strong dependence on mass transport to the electrode on the flow rate (and the channel cross section). Recently, we investigated the effect of the flow rate on the performance of a nanofluidic sensor located in a microchannel [39].

For this study, the nanogap sensor was located at the bottom of a microchannel (3 mm length, 200 μm height and 300 μm in width), a

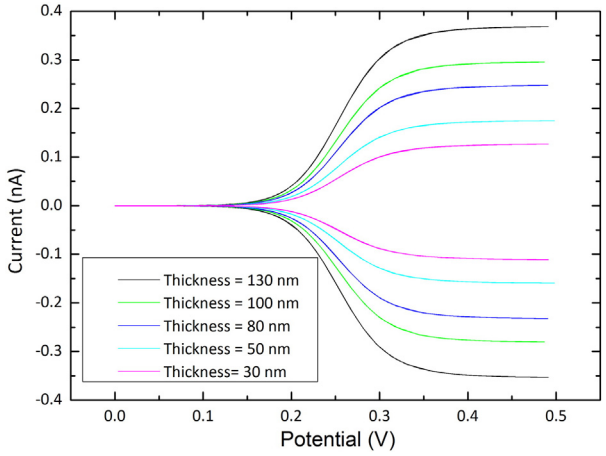

Fig. 4. Cyclic voltammograms (scan rate: 10 mV s^{-1}) showing the effect of different electrode thicknesses on the redox cycling current (the collector electrode is kept constant potential of 0 V).

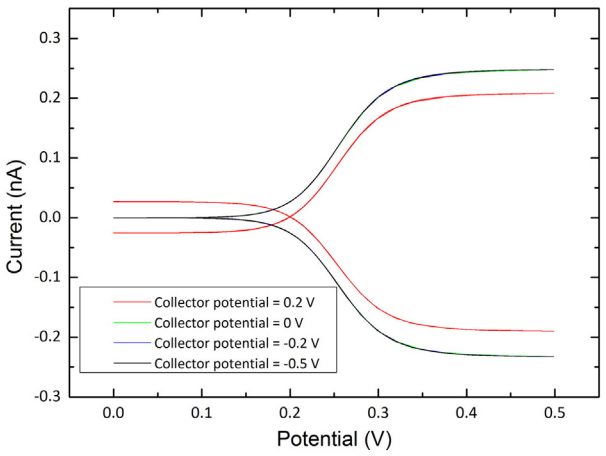

Fig. 5. Cyclic voltammograms showing the effect of different collector potentials. The generator electrode is swept between 0 and 0.5 V (scan rate: 10 mV s^{-1}); the collector electrode is kept at different constant potentials.

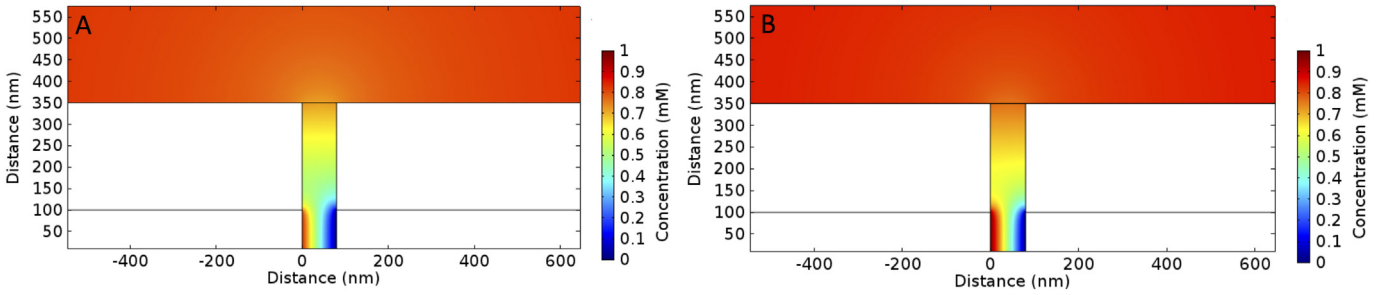

Fig. 6. Concentration profile for the reduced species in a 80 nm nanogap device with a 250 nm isolating layer. The right electrode is set at 0.5 V, and the left electrode is set at (A) 0.2 V and (B) 0 V. The nanogap device connects to a reservoir on top with a bulk concentration of 1 mM $Fc(MeOH)_2$.

laminar flow was introduced perpendicular to the nanogap (*i.e.*, from left to right for the representation in Fig. 6). We evaluated the flow profile by using the Stokes equations for an incompressible fluid.

$$\vec{\nabla}p = \eta\nabla^2\vec{u}, \quad \vec{\nabla}\cdot\vec{u} = 0. \tag{7}$$

Here $\vec{u}$ is the flow velocity, p is the hydrostatic pressure, and η is the dynamic viscosity (0.001 Pa·s for water). We chose the boundary conditions of a constant laminar inflow rate at the microchannel inlet, $p =$ 0 Pa at the outlet, and no-slip conditions for all other boundaries. The redox cycling current was determined as a function of flow ranging from rates of 0 to 600 μl s^{-1} for the flow profile in the microchannel for a 80 nm nanogap (with a 250 nm isolating layer and 80 nm electrode thickness). Fig. 7A presents cyclic voltammograms for various flow rates. At the center of the channel floor, these rates correspond to shear rates (flow velocity gradients ranging from 0 to 8600 s^{-1} as determined by $\frac{\partial}{\partial z}v_x(z=0) = \frac{6}{h^2w-0.63h^3}Q$. (Here, $\partial v_x/\partial z$ is the shear rate [40], Q is volume flow rate, h and w are the height and width of the microchannel, respectively.)

Previously, we showed that increasing the flow rate in a microchannel on top of a nanofluidic gap sensor does not affect the redox cycling signal [39,41]. Since diffusion of species between the electrodes in nanogap is fast in redox cycling, a variation of flow rate in micro-channel – considering also the large hydrodynamic resistance of the nanogap – does not alter the redox cycling current. Fig. 7A reveals that, even with the open nanochannel geometry studied here, the electrochemical redox cycling currents are unaffected by a change in flow rate in the microfluidic channel.

Ultimately, we studied the effect of flow rate combined with one of the most important parameter in geometric design: gap size. For this purpose, we defined a device with a wide gap of 170 nm (see Fig. 7B). The nanogap device clearly is sensitive to the variation of flow rate once the gap size is expanded to 170 nm. In this situation, the flow rate affects both the limiting current and the collection efficiency (the collection efficiency reduces from 0.85 to 0.76 by increasing the flow rate from 0 to 600 μl s^{-1}). Here, the flow prevents inter-diffusion of species between the two electrodes.

4. Conclusion

We proposed a new design for generator-collector nanogap devices and performed finite element simulations to study electrochemical processes inside the sensor. We considered the effect of different geometric parameters as well as applied potentials for this design. Data revealed that decreasing the gap size and increasing the electrode thickness increase the amplification factor and collection efficiency of the device. However, varying the thickness of the top isolating layer results in insignificant changes in the device performance. We also showed that, once the nanogap is located in a microfluidic channel, for small gap sizes (<170 nm) a change in flow rate typical for microfluidic channels does not influence the electrochemical processes in the gap. This information can be utilized for the fabrication of these nanogap sensors and their use in electroanalytical applications.

These sensors will combine the advantages of ease of fabrication, intrinsic high signal amplification due to redox cycling and possible integration into lab-chip or point-of-care devices. The independence of flow rate enhances the reliability in such applications as a calibration method

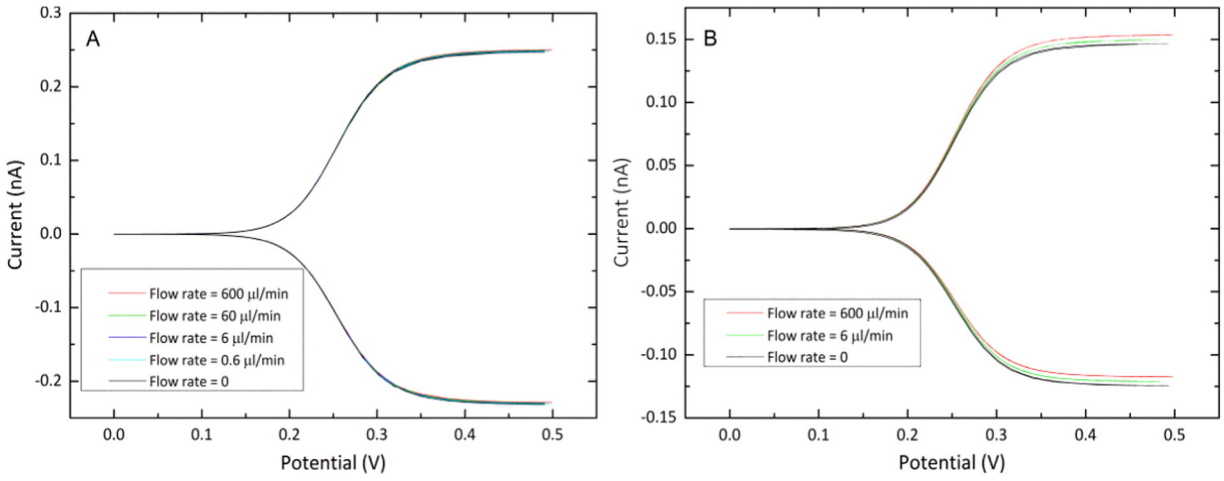

Fig. 7. Cyclic voltammograms (scan rate: 10 mV s^{-1}) showing the effect of flow rate on the redox cycling current in the nanogap with (A) 80 nm gap size and (B) 170 nm gap size located in a microchannel. The potential of the generator electrode was swept between 0 and 0.5 V and the potential of collector electrode was kept constant at 0 V.

is not required. Moreover, the open design will allow the combination with different detection techniques such as optical microscopy.

The simulations and well-understood geometry will enable a straightforward detailed and quantitative assessment of future experimental data.

References

[1] J.T. Cox, B. Zhang, Nanoelectrodes: recent advances and new directions, Annu. Rev. Anal. Chem. 5 (2012) 253–272.
[2] K. Mathwig, T. Albrecht, E.D. Goluch, L. Rassaei, Challenges of Biomolecular detection at the nanoscale: nanopores and Microelectrodes, Anal. Chem. (2015) (DOI).
[3] H. Ben-Yoav, T.E. Winkler, E. Kim, S.E. Chocron, D.L. Kelly, G.F. Payne, R. Ghodssi, Redox cycling-based amplifying electrochemical sensor for in situ clozapine antipsychotic treatment monitoring, Electrochim. Acta 130 (2014) 497–503.
[4] K. Ino, Y. Kanno, T. Nishijo, H. Komaki, Y. Yamada, S. Yoshida, Y. Takahashi, H. Shiku, T. Matsue, Densified electrochemical sensors based on local redox cycling between vertically separated electrodes in substrate generation/chip collection and extended feedback modes, Anal. Chem. 86 (2014) 4016–4023.
[5] A. Walter, J. Wu, G.-U. Flechsig, D.A. Haake, J. Wang, Redox cycling amplified electrochemical detection of DNA hybridization: application to pathogen *E. coli* bacterial RNA, Anal. Chim. Acta 689 (2011) 29–33.
[6] W.J. Albery, M.L. Hitchman, Ring-disc Electrodes, Oxford University Press, 1971.
[7] W. Albery, M. Hitchman, J. Ulstrup, Ring-disc electrodes. Part 9.—application to first-order kinetics, Trans. Faraday Soc. 64 (1968) 2831–2840.
[8] C. Amatore, C. Sella, L. Thouin, Electrochemical time-of-flight responses at double-band generator-collector devices under pulsed conditions, J. Electroanal. Chem. 593 (2006) 194–202.
[9] P. Liljeroth, C. Johans, C.J. Slevin, B.M. Quinn, K. Kontturi, Micro ring–disk electrode probes for scanning electrochemical microscopy, Electrochem. Commun. 4 (2002) 67–71.
[10] C. Thomas, P. Springer, G. Loeb, Y. Berwald-Netter, L. Okun, A miniature microelectrode array to monitor the bioelectric activity of cultured cells, Exp. Cell Res. 74 (1972) 61–66.
[11] A. van den Berg, Redox cycling with facing interdigitated array electrodes as a method for selective detection of redox species, Analyst 132 (2007) 365–370.
[12] I.J. Cutress, Y. Wang, J.G. Limon-Petersen, S.E. Dale, L. Rassaei, F. Marken, R.G. Compton, Dual-microdisk electrodes in transient generator–collector mode: experiment and theory, J. Electroanal. Chem. 655 (2011) 147–153.
[13] L. Rassaei, R.W. French, R.G. Compton, F. Marken, Microwave-enhanced electroanalytical processes: generator–collector voltammetry at paired gold electrode junctions, Analyst 134 (2009) 887–892.
[14] E.O. Barnes, G.E. Lewis, S.E. Dale, F. Marken, R.G. Compton, Generator-collector double electrode systems: a review, Analyst 137 (2012) 1068–1081.
[15] R.W. French, S.N. Gordeev, P.R. Raithby, F. Marken, Paired gold junction electrodes with submicrometer gap, J. Electroanal. Chem. 632 (2009) 206–210.
[16] D. Mampallil, K. Mathwig, S. Kang, S.G. Lemay, Redox couples with unequal diffusion coefficients: effect on redox cycling, Anal. Chem. 85 (2013) 6053–6058.
[17] R.W. French, A.M. Collins, F. Marken, Growth and application of paired gold electrode junctions: evidence for nitrosonium phosphate during nitric oxide oxidation, Electroanalysis 20 (2008) 2403–2409.
[18] D. Menshykau, M. Cortina-Puig, F.J. del Campo, F.X. Muñoz, R.G. Compton, Plane-recessed disk electrodes and their arrays in transient generator–collector mode: the measurement of the rate of the chemical reaction of electrochemically generated species, J. Electroanal. Chem. 648 (2010) 28–35.
[19] L. Rassaei, P.S. Singh, S.G. Lemay, Lithography-based nanoelectrochemistry, Anal. Chem. 83 (2011) 3974–3980.
[20] S.E. Dale, A. Vuorema, M. Sillanpää, J. Weber, A.J. Wain, E.O. Barnes, R.G. Compton, F. Marken, Nano-litre proton/hydrogen titration in a dual-plate platinum–platinum generator–collector electrode micro-trench, Electrochim. Acta 125 (2014) 94–100.
[21] M.A. Hasnat, A.J. Gross, S.E. Dale, E.O. Barnes, R.G. Compton, F. Marken, A dual-plate ITO–ITO generator–collector microtrench sensor: surface activation, spatial separation and suppression of irreversible oxygen and ascorbate interference, Analyst 139 (2014) 569–575.
[22] A.J. Gross, S. Holmes, S.E. Dale, M.J. Smallwood, S.J. Green, C.P. Winlove, N. Benjamin, P.G. Winyard, F. Marken, Nitrite/nitrate detection in serum based on dual-plate generator–collector currents in a microtrench, Talanta 131 (2015) 228–235.
[23] M.A. Zevenbergen, B.L. Wolfrum, E.D. Goluch, P.S. Singh, S.G. Lemay, Fast electron-transfer kinetics probed in nanofluidic channels, J. Am. Chem. Soc. 131 (2009) 11471–11477.
[24] B. Wolfrum, M. Zevenbergen, S. Lemay, Nanofluidic redox cycling amplification for the selective detection of catechol, Anal. Chem. 80 (2008) 972–977.
[25] M.A. Zevenbergen, P.S. Singh, E.D. Goluch, B.L. Wolfrum, S.G. Lemay, Stochastic sensing of single molecules in a nanofluidic electrochemical device, Nano Lett. 11 (2011) 2881–2886.
[26] K. Mathwig, T.J. Aartsma, G.W. Canters, S.G. Lemay, Nanoscale methods for single-molecule electrochemistry, Annu. Rev. Anal. Chem. 7 (2014) 383–404.
[27] L. Rassaei, K. Mathwig, S. Kang, H.A. Heering, S.G. Lemay, Integrated biodetection in a nanofluidic device, ACS Nano 8 (2014) 8278–8284.
[28] E.D. Goluch, B. Wolfrum, P.S. Singh, M.A. Zevenbergen, S.G. Lemay, Redox cycling in nanofluidic channels using interdigitated electrodes, Anal. Bioanal. Chem. 394 (2009) 447–456.
[29] C. Ma, N.M. Contento, L.R. Gibson, P.W. Bohn, Redox cycling in nanoscale-recessed ring-disk electrode arrays for enhanced electrochemical sensitivity, ACS Nano 7 (2013) 5483–5490.
[30] S.K. Kim, P.J. Hesketh, C. Li, J.H. Thomas, H.B. Halsall, W.R. Heineman, Fabrication of comb interdigitated electrodes array (IDA) for a microbead-based electrochemical assay system, Biosens. Bioelectron. 20 (2004) 887–894.
[31] R.R. Kamath, M.J. Madou, Three-dimensional carbon interdigitated electrode arrays for redox-amplification, Anal. Chem. 86 (2014) 2963–2971.
[32] J. Heo, D. Shim, G.T. Teixidor, S. Oh, M. Madou, H. Shin, Carbon interdigitated array nanoelectrodes for electrochemical applications, J. Electrochem. Soc. 158 (2011) J76–J80.
[33] K.V. Singh, A.M. Whited, Y. Ragineni, T.W. Barrett, J. King, R. Solanki, 3D nanogap interdigitated electrode array biosensors, Anal. Bioanal. Chem. 397 (2010) 1493–1502.
[34] A.J. Bard, L.R. Faulkner, Electrochemical Methods: Fundamentals and Applications, Wiley, New York, 1980.
[35] X. Yang, G. Zhang, The voltammetric performance of interdigitated electrodes with different electron-transfer rate constants, Sensors Actuators B Chem. 126 (2007) 624–631.
[36] J. Min, A.J. Baeumner, Characterization and optimization of interdigitated ultramicroelectrode arrays as electrochemical biosensor transducers, Electroanalysis 16 (2004) 724–729.
[37] L.B. Anderson, C.N. Reilley, Thin-layer electrochemistry: steady-state methods of studying rate processes, J. Electroanal. Chem. 10 (1965) (1959) 295–305.
[38] M. Straver, M. Odijk, W. Olthuis, A. van den Berg, A simple method to fabricate electrochemical sensor systems with predictable high-redox cycling amplification, Lab Chip 12 (2012) 1548–1553.
[39] L. Rassaei, K. Mathwig, E.D. Goluch, S.G. Lemay, Hydrodynamic voltammetry with nanogap electrodes, J. Phys. Chem. C 116 (2012) 10913–10916.
[40] H. Bruus, Acoustofluidics 1: governing equations in microfluidics, Lab Chip 11 (2011) 3742–3751.
[41] K. Mathwig, S.G. Lemay, Mass transport in electrochemical nanogap sensors, Electrochim. Acta 112 (2013) 943–949.